

# A Parallelized Coupled Navier-Stokes/Vortex-Panel Solver

**Sven Schmitz**

Graduate Student Researcher  
e-mail: shschmitz@ucdavis.edu

**Jean-Jacques Chattot**

Professor  
e-mail: jjchattot@ucdavis.edu

Department of Mechanical and Aeronautical  
Engineering, University of California Davis, One  
Shields Ave, Davis, CA 95616-5294

*A Navier-Stokes solver, CFX V5.6, is coupled with an in-house developed Vortex-Panel method for the numerical analysis of wind turbines. The Navier-Stokes zone is confined to the near-field around one wind turbine blade, the Vortex-Panel method models the entire vortex sheet of a two-bladed rotor and accounts for the far-field. This coupling methodology reduces both numerical diffusion and computational cost. The parallelized coupled solver (PCS) is applied to the NREL Phase VI rotor configuration under no-yaw conditions. Fully turbulent flow is assumed using the  $k-\epsilon$  and  $k-\omega$  turbulence models. Results obtained are very encouraging for fully attached flow. For separated and partially stalled flow, results are in good agreement with experimental data. Discrepancies observed between the turbulence models are attributed to different prediction of the onset of separation. This is revealed by two-dimensional (2D) results of the S809 airfoil.*

[DOI: 10.1115/1.2035707]

## Introduction

The Unsteady Aerodynamic Experiment (UAE) conducted by NREL for the Phase VI Rotor configuration provides an excellent database for the design and validation of computational models [1]. A Blind Comparison between different classes of computational tools and measured data showed a wide spread in results obtained [2]. However, full three-dimensional (3D) Navier-Stokes (NS) simulations performed by Sørensen et al. [3–5] showed best agreement with experimental data at the original blind comparison. Since then, a number of NS simulations have been documented in Europe and in the U.S., e.g., Sankar et al. [6,7], Le Pape et al. [8], and Duque et al. [9]. Nevertheless, Blade Element Models (BEM) as well as Wake Models (WM) showed fairly good agreement with experimental data at low wind speeds, whereas Aeroelastic Models (AM) exhibited the widest spread in computational results. A Helicoidal Vortex Model with a lifting line and a rigid wake has been developed by Chattot [10,11] and gives good results for conditions where the flow along the blade is fully attached or moderately separated. A common advantage of all vortex line models (VLM) is their ability to convect shed vorticity into the wake with very little dissipation. This is a good approximation, as the Reynolds number for the blade is in the order of  $10^5$ – $10^6$ . It can be seen from Fig. 1 that the convection of vortical structures far into the wake is indeed important. Moreover, a VLM can easily account for blade interaction. These are some major advantages compared to BEM codes, which have been previously reported by Tangler [12]. However, a VLM cannot predict strong three-dimensional effects near the tips or if large separated regions exist on the blade. On the other hand, a NS solver is capable of resolving such three-dimensional flow features in the vicinity of the blade, yet it dissipates vortical structures rapidly in the wake, which is unphysical. Higher-order discretization schemes as well as vorticity confinement due to Steinhoff [13] can reduce artificial dissipation, however, at a much higher computational cost. A novel approach has been developed confining the NS solver to a small region in the immediate vicinity of the blade and coupling it with a Vortex-Panel method (VPM) to account for the far-field. This reduces both artificial dissipation and computational cost.

The approach has been validated by the authors in [14] for fully attached flow around an optimal wind turbine blade.

## Numerical Methods

**Coupling Methodology.** The methodology of the Parallelized Coupled Solver (PCS) is shown in Fig. 2. Starting with an undisturbed flow consisting of wind speed and blade rotation entrainment speed, the NS code solves for the flow field around one wind turbine blade, see Fig. 3(a). Inside the NS region, the circulation at each radial station is determined by performing a line integral with the contour  $L_j$  including all sources of vorticity, namely the boundary layer. This is revealed through Stokes' theorem in Fig. 2. The VPM distributes  $\Gamma_j$  along a bounding vortex and the trailing vorticity  $\delta\Gamma_j$  along a rigid wake. The rigid wake includes the entire vortex sheet consisting of root vortex, inboard vortex sheet, and tip vortex. This is an important difference with the hybrid method of Sankar et al. [6,7] and Benjanirat and Sankar [15], where solely the tip vortex or a combination of tip and root vortices are modeled. The bounding vortex and the trailing vortex sheet of the second rotor blade are modeled with symmetry conditions. Therefore, this coupling methodology can only be applied to zero-yaw conditions at the present stage. Induced velocities of the vortex systems of both blades are calculated by a discrete form of the Biot-Savart law and are imposed as outer boundary conditions to the NS region for the next coupling step. Coupling is performed after each 10–20 accumulated time steps of the NS solver. The coupling is regarded as converged, if the change in  $\Gamma_j$  is less than  $10^{-5}$ . This is usually achieved after 3–5 coupling steps.

**Navier-Stokes Zone.** CFX V5.6 is used as the NS solver. The code uses a finite-volume higher order discretization technique combined with an algebraic multigrid method. The flow is assumed to be steady and fully turbulent. The  $k-\epsilon$  as well as  $k-\omega$  two-equation turbulence models are used for the analysis. The rotor blade is meshed with 120 points along its contour, 50 points in the wake, and 40 points in the spanwise direction. The tip shapes of the NREL Phase VI rotor are not modeled. The blunt blade tips are meshed with an unstructured Delaunay surface mesher and extruded as prisms to the boundaries of the NS zone, see Fig. 3. A wake plane originates from the blade's trailing edge. It is aligned with the first  $60^\circ$  of azimuth of the vortex sheet created by the vortex model such that vortex filaments in Fig. 2 pass between nodes. This ensures that induced velocities obtained

Contributed by the Solar Energy Division and presented at the 24th ASME Wind Energy Symposium, Reno, Nevada of THE AMERICAN SOCIETY OF MECHANICAL ENGINEERS. Manuscript received by the ASME Solar Division January 28, 2005; final revision May 30, 2005. Associate Editor A. Steinfeld.



Fig. 1 NREL Phase VI Rotor (NREL)

by the vortex model are smooth along the boundary of the NS zone. A C-type structured mesh of 45–55 layers with 10–15 layers inside the boundary layer is extruded upon the blade, extruded tips, and wake plane using hyperbolic functions. The mesh shown in Fig. 3 is designed in such a way that the trailing vortex sheet of the second blade does not cut the NS zone. The Navier-Stokes zone extends from 2 to 3 mean chord lengths around the blade and 3–6 mean chord lengths into the wake. The hybrid mesh inside the NS zone contains a total of approximately 800,000 nodes. Near-wall treatment is handled by scalable wall functions. The main advantage of the wall function approach is that high gradient shear layers near walls can be modeled with relatively coarse meshes, thus not requiring prohibitively fine meshes with a large number of nodes. This yields substantial savings in CPU time and storage. In the scalable wall function approach, the surface coincides with the edge of the viscous sublayer, i.e.,  $y^+ = 11$ , and computed  $y^+$  values are not allowed to fall below this limit. This eliminates fine grid inconsistencies of traditional wall functions, see Grotjans and Menter [16]. The NS solver is parallelized on a cluster of 4 processors showing higher than 90% efficiencies. The algorithm Me-Tis by Karypis and Kumar [17] is used for partitioning.

**Vortex-Panel Method.** Induced velocities at an arbitrary point  $\mathbf{c} = (x_c, y_c, z_c)^T$  on the outer boundary of the Navier-Stokes zone are obtained using the Biot-Savart law.

$$\mathbf{v}_c = (u_c, v_c, w_c)^T = \int \frac{\Gamma}{4\pi} \cdot \frac{\mathbf{dl} \times \mathbf{r}}{r^3} \quad (1)$$

Equation (1) is written in discrete form for Cartesian velocity components adding the contributions of vortex sheets and bound vortices

$$\begin{aligned} u_c &= \frac{1}{4\pi} \sum_{j=1}^{jx} \delta\Gamma_j \cdot (a_j^{\text{helix}} + a_{j,\text{rem}}^{\text{helix}}) + \bar{\Gamma}_j \cdot a_j^{\text{bound}} \\ v_c &= \frac{1}{4\pi} \sum_{j=1}^{jx} \delta\Gamma_j \cdot (b_j^{\text{helix}} + b_{j,\text{rem}}^{\text{helix}}) \\ w_c &= \frac{1}{4\pi} \sum_{j=1}^{jx} \delta\Gamma_j \cdot (c_j^{\text{helix}} + c_{j,\text{rem}}^{\text{helix}}) + \bar{\Gamma}_j \cdot c_j^{\text{bound}} \end{aligned} \quad (2)$$

where the subscript  $j$  denotes the spanwise location on the blade and  $a, b, c$  are geometric influence coefficients for a two-bladed rotor, which are defined later. Length scales are nondimensionalized by the blade radius  $R$ , velocity scales by the wind speed

$V_{\text{Wind}}$ .

**Bound Vortex.** At this stage, all vortex panels on the blade are lumped into one bound vortex that is located on the  $y$  axis. The bound vortex consists of  $jx$  vortex filaments, each filament being of constant strength and divided into  $kx=5$  pieces of length  $\Delta l_{k,j} = (y_j - y_{j-1})/kx$ . This repartition is performed, because the Biot-Savart integral in Eq. (1) is evaluated numerically. Thus, it allows accurate calculation of induced velocities. The strength of each bound vortex filament is the arithmetic average of the neighboring values for the circulation  $\Gamma_{j-1}$  and  $\Gamma_j$  obtained from the line integral along contour  $L_j$ , see Fig. 4(a). The influence coefficients in Eq. (2) thus become

$$\begin{aligned} a_j^{\text{bound}} &= \sum_{k=1}^{kx} \frac{(z_c - z_{k,j}) \cdot \Delta y_{k,j}}{[x_c^2 + (y_c - y_{k,j})^2 + z_c^2]^{3/2}} \Big|_{\text{Blade } I,II} \\ c_j^{\text{bound}} &= \sum_{k=1}^{kx} \frac{(x_c - x_{k,j}) \cdot \Delta y_{k,j}}{[x_c^2 + (y_c - y_{k,j})^2 + z_c^2]^{3/2}} \Big|_{\text{Blade } I,II} \end{aligned} \quad (3)$$

with  $b_j^{\text{bound}} = 0$ , as the bound vortex lies on the  $y$  axis.

**Helicoidal Vortex Filament.** The vortex sheet is described in a rotating frame of reference. A total of  $jx$  vortex filaments originates from the blade's trailing edge at locations  $y_{j-1/2}$ . Figure 4(b) shows one vortex filament trailing downstream of the blade. Each vortex filament is divided into  $ix$  pieces of lengths  $\Delta l_{i,j}$ . It is helpful to use polar coordinates to describe the location of each piece of vortex filament and the vortex sheet.

$$x_{i,j} = x_{\text{TE},j} + x_i$$

$$y_{i,j} = r_j \cdot \cos(x_i / \text{adv}_i + \varphi_j) \quad (4)$$

$$z_{i,j} = r_j \cdot \sin(x_i / \text{adv}_i + \varphi_j)$$

where  $r_j$  and  $\varphi_j$  are radius and phase angle of the trailing edge in the  $(x, y)$  plane. In Eq. (4),  $\text{adv}_i = (V_{\text{Wind}} + u_i(x_i)) / (\Omega^* R)$  is defined as the advance ratio with  $V_{\text{Wind}}$  being the wind speed,  $u_i$  the local axial induced velocity,  $\Omega$  the angular rotor speed, and  $R$  the blade radius. As a wind turbine extracts energy from the main flow, the pitch of the helicoidal vortex sheet decreases, while the stream tube expands. The advance ratio controls the pitch of the helix; its value at the blade  $\text{adv}_B = (V_{\text{Wind}} + u_B) / (\Omega^* R)$  is obtained from the actuator disk power estimate as  $P = 2\pi\rho R^2 (V_{\text{Wind}} + u_B)^2 u_B$ . The advance ratio of the Trefftz plane  $\text{adv}_T = (V_{\text{Wind}} + u_T) / (\Omega^* R)$ , where  $u_B = 0.5u_T < 0$ , is reached after 4 blade radii downstream of the blade and remains constant thereafter. The local axial induced velocity  $u_i$  varies linearly between  $u_B$  and  $u_T$ . The expansion of the stream tube is neglected. In Eq. (4),  $x_i$  describes the step size in  $x$  direction, respectively, vortex segmentation  $\Delta\Theta_i [\text{rad}] = x_i / \text{adv}_i$ . An illustration of the vortex segmentation is given in Fig. 2. The variable step size  $x_i$ , respectively, vortex segmentation  $\Delta\Theta_i$ , is important for the accuracy of calculated induced velocities, see also Gupta and Leishman [18]. Letting

$$|\mathbf{r}_c - \mathbf{r}_{i,j}| = [(x_c - x_{i,j})^2 + (y_c - y_{i,j})^2 + (z_c - z_{i,j})^2]^{1/2} \quad (5)$$

be the distance between a piece of vortex filament and the arbitrary point  $C$ , the influence coefficients of the helicoidal vortex sheets in Eq. (2) become

$$\begin{aligned} a_j^{\text{helix}} &= \sum_{i=2}^{ix} \frac{(z_c - z_{i,j}) \cdot \Delta y_{i,j} - (y_c - y_{i,j}) \cdot \Delta z_{i,j}}{|\mathbf{r}_c - \mathbf{r}_{i,j}|^3} \Big|_{\text{Blade } I,II} \\ b_j^{\text{helix}} &= \sum_{i=2}^{ix} \frac{(x_c - x_{i,j}) \cdot \Delta z_{i,j} - (z_c - z_{i,j}) \cdot \Delta x_{i,j}}{|\mathbf{r}_c - \mathbf{r}_{i,j}|^3} \Big|_{\text{Blade } I,II} \end{aligned} \quad (6)$$

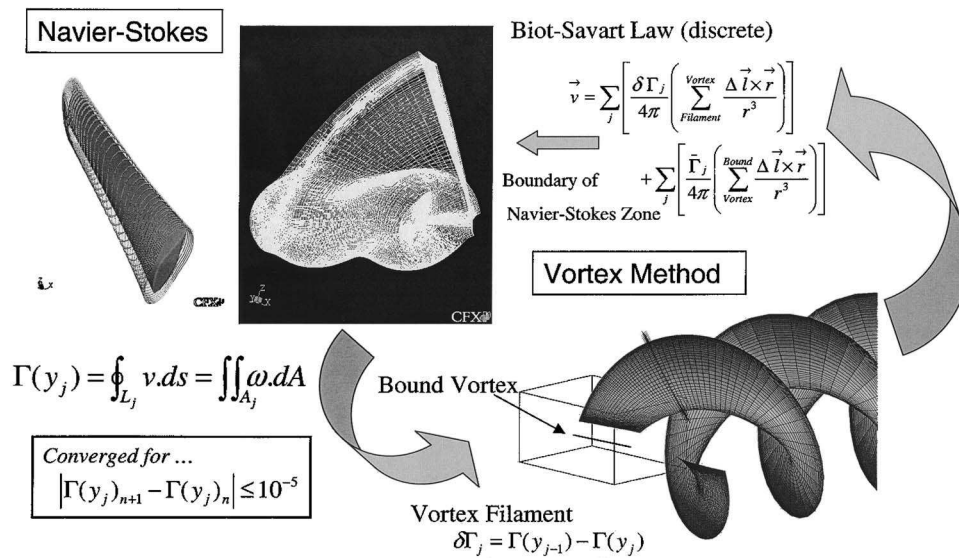


Fig. 2 Methodology of coupled solver

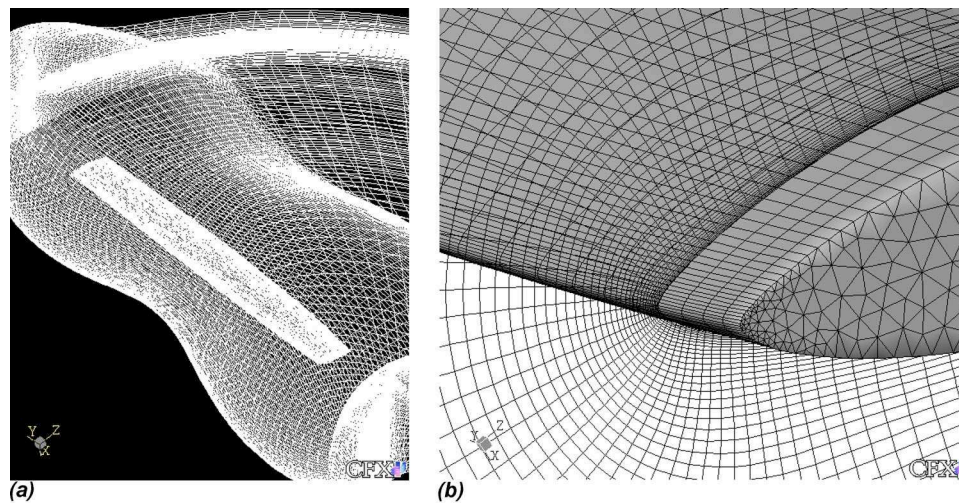


Fig. 3 (a) NS zone; (b) Grid detail at blade tip

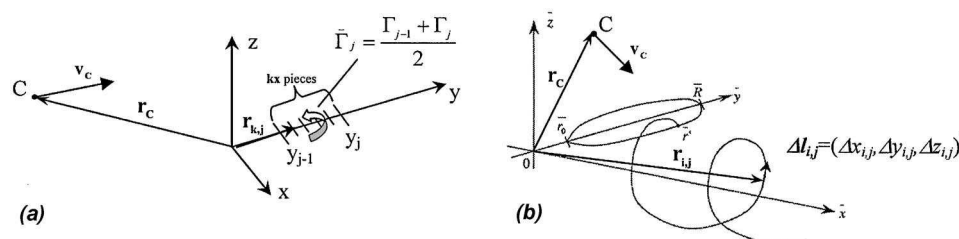


Fig. 4 (a) Bound vortex; (b) Helicoidal vortex filament



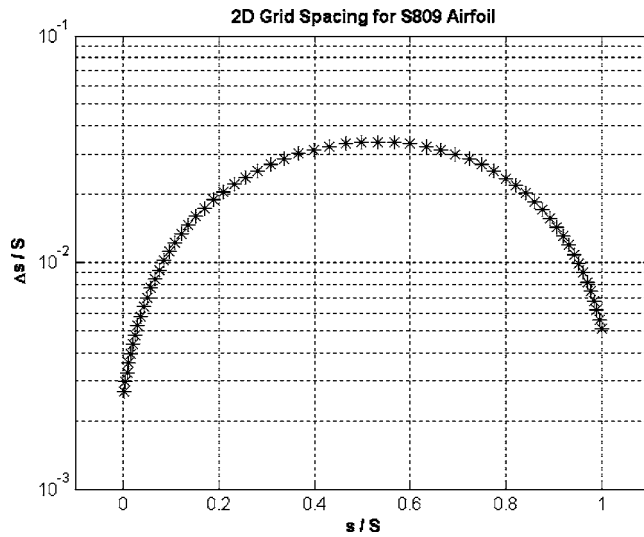


Fig. 5 2D grid spacing (60 points)

$$c_j^{\text{helix}} = \sum_{i=2}^{ix} \frac{(y_C - y_{i,j}) \cdot \Delta x_{i,j} - (x_C - x_{i,j}) \cdot \Delta y_{i,j}}{|\mathbf{r}_C - \mathbf{r}_{i,j}|^3} \Big|_{\text{Blade I,II}}$$

Remainder terms in Eq. (2) are obtained from an asymptotic integral relation

$$\begin{aligned} a_{j,\text{rem}}^{\text{helix}} &= \int_{x_{ix,j}}^{\infty} \frac{(z_C - z_{i,j}) \cdot dy_{i,j} - (y_C - y_{i,j}) \cdot dz_{i,j}}{x_{i,j}^3} \Big|_{\text{Blade I,II}} \\ b_{j,\text{rem}}^{\text{helix}} &= \int_{x_{ix,j}}^{\infty} \frac{-x_{i,j} \cdot dz_{i,j} - (z_C - z_{i,j}) \cdot dx_{i,j}}{x_{i,j}^3} \Big|_{\text{Blade I,II}} \\ c_{j,\text{rem}}^{\text{helix}} &= \int_{x_{ix,j}}^{\infty} \frac{(y_C - y_{i,j}) \cdot dx_{i,j} + x_{i,j} \cdot dy_{i,j}}{x_{i,j}^3} \Big|_{\text{Blade I,II}} \end{aligned} \quad (7)$$

with  $x_{i,j} \gg \{x_C, y_C - y_{i,j}, z_C - z_{i,j}\}$ . Substituting the differentials  $dy_{i,j}$  and  $dz_{i,j}$  in Eq. (7) by using Eq. (4), integration by parts leads to

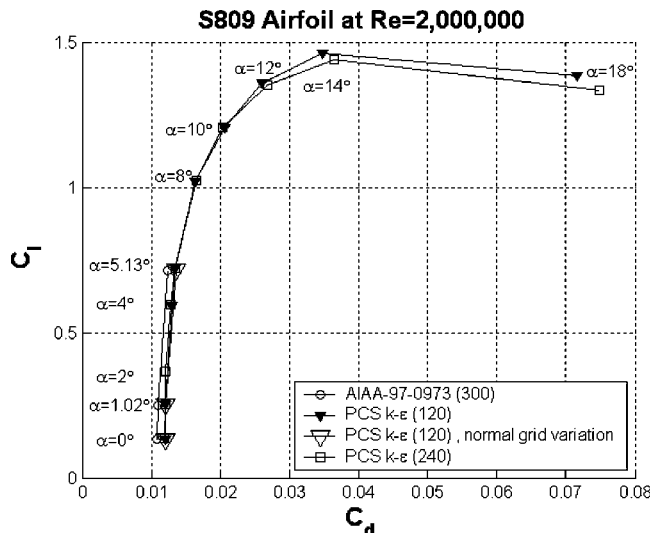


Fig. 6 S809 profile polar (grid convergence)

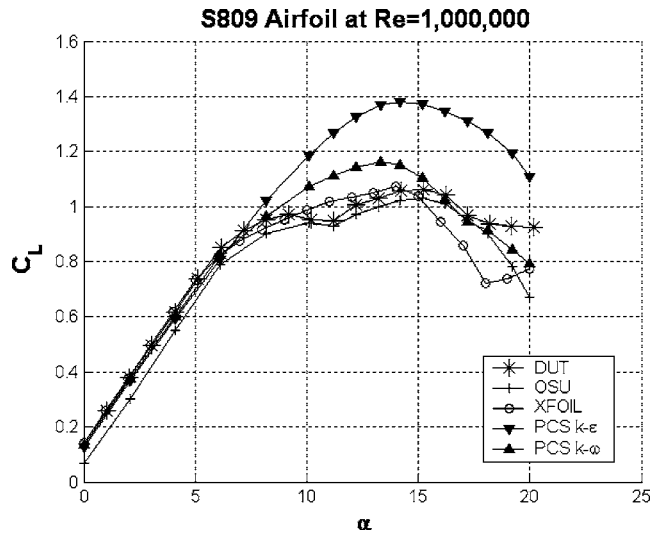


Fig. 7 Lift coefficient for S809 airfoil

$$\begin{aligned} a_{j,\text{rem}}^{\text{helix}} &= \frac{r_j^2}{\text{adv}_T \cdot x_{T,j}^2}; \quad b_{j,\text{rem}}^{\text{helix}} = \frac{z_C - 2r_j \sin(x_{T,j}/\text{adv}_T)}{x_{T,j}^2}; \\ c_{j,\text{rem}}^{\text{helix}} &= \frac{y_C - 2r_j \cos(x_{T,j}/\text{adv}_T)}{x_{T,j}^2} \end{aligned} \quad (8)$$

where higher order terms  $O(1/x_{T,j}^3)$  have been neglected. In Eq. (8),  $x_{T,j} = x_{ix,j}$  is the location of the Trefftz plane typically set at approximately 20 blade radii downstream of the rotor disc. The terms in Eq. (8) are then 2 orders of magnitude smaller than those in Eq. (6). As induced velocities in Eq. (2) serve as boundary conditions for the Navier-Stokes zone, it is essential to calculate them as accurately as possible. The following list summarizes the parameters involved in accurate calculation of induced velocities.

- Vortex Segmentation  $\Delta\Theta_i$ :  $0.02^\circ$  at the blade,  $12^\circ$  after 1 revolution
- Trefftz Plane Location: 20 blade radii behind the rotor disc
- Minimum Number of Vortex Filaments: 39

Refinement of all parameters revealed that induced velocities can

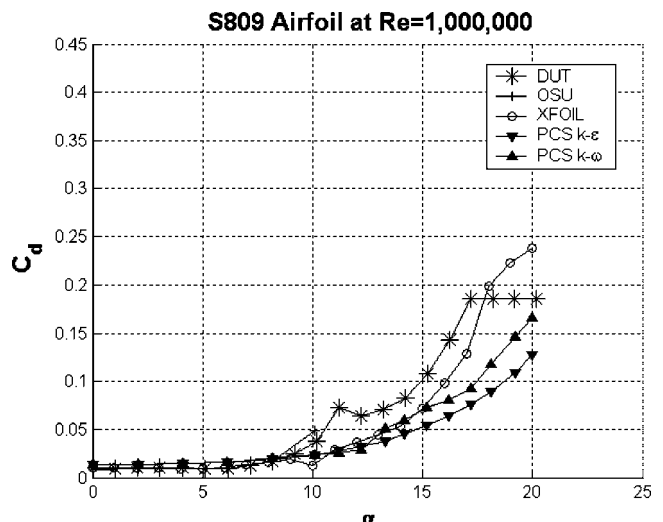


Fig. 8 Drag coefficient for S809 airfoil

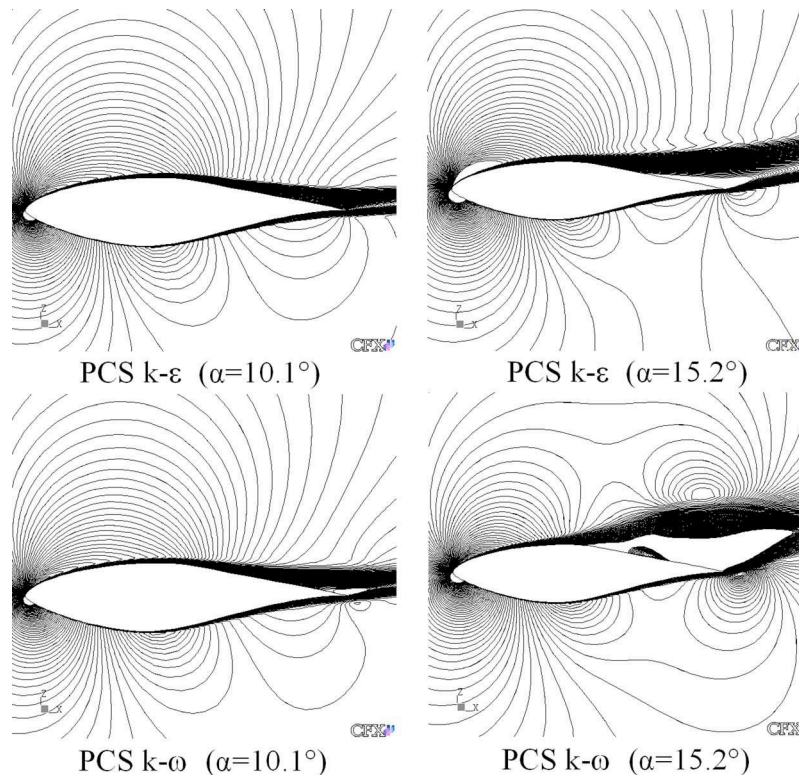


Fig. 9 U-contours for S809 airfoil

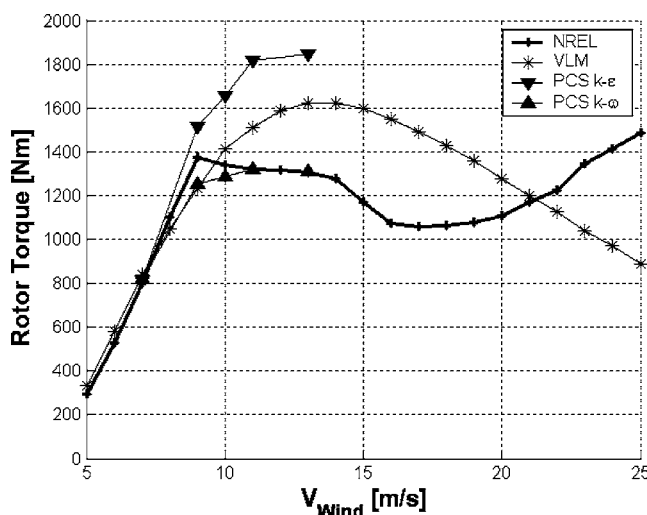


Fig. 10 Torque vs wind speed (NREL phase VI, no yaw)

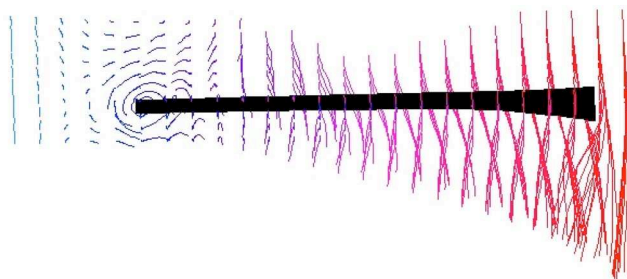


Fig. 11 Streamlines in front of blade ( $V_{Wind}=7$  m/s) TIP=left, ROOT=right



Fig. 12 Isosurface of vorticity ( $V_{Wind}=7$  m/s)

be predicted within 2% of their values anywhere on the outer surface of the NS zone. It should be kept in mind that the vortex roll-up is not considered in the vortex panel method. The roll-up is known to affect tip loads and is accompanied with an expansion of the stream tube behind the rotor, which is also neglected in the present model as stated earlier. However, the near-field is accurately resolved by the NS solver, while the rigid wake model affects the flow solution in terms of induced velocities, which are imposed as boundary conditions a few mean chord lengths away from the blade. Therefore, neglecting vortex roll-up and stream tube expansion can be regarded as a higher order effect, which does not alter the vorticity content, only distributes it slightly differently.

## Results and Discussion

**2D Calculations of the S809 Airfoil.** The S809 airfoil is 21% thick with 1% camber and a leading edge radius of less than 1%. The small leading edge radius makes it particularly difficult to capture the stagnation point location and the suction peak on the upper surface. Due to computer storage constraints for the full 3D calculations, a total of 120 points could be afforded along the airfoil contour. Figure 5 illustrates the grid spacing  $\Delta s$  with respect to the total arc length  $S$  of either upper or lower airfoil

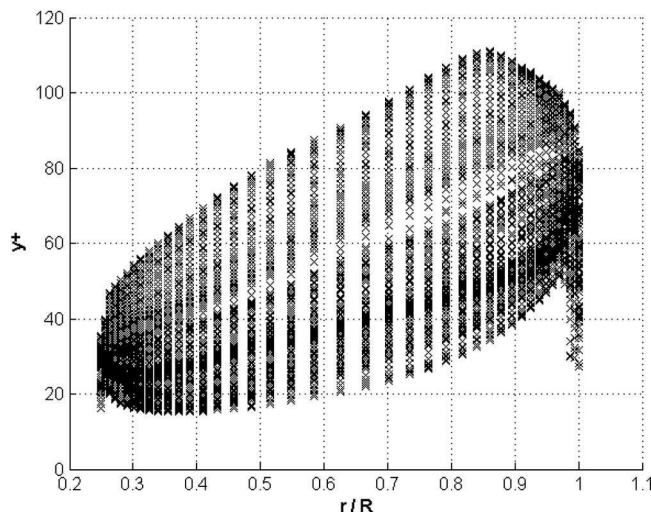


Fig. 13 Nondimensional wall distance  $y^+$  ( $V_{\text{Wind}}=7$  m/s)

contour. Fully turbulent  $k-\epsilon$  computations of the S809 airfoil were performed by Wolfe and Ochs [19] for a Reynolds number of  $Re=2 \times 10^6$  and fully attached flow ( $0^\circ \leq \alpha \leq 5.13^\circ$ ). Results obtained with the PCS solver using 120 points along the airfoil contour show good agreement with data from Wolfe and Ochs and are shown in Fig. 6. Values for the lift coefficient differ by less than

1.5%, while values for the drag coefficient show a larger discrepancy of up to 8%. In Fig. 6, the numbers in parentheses denote the number of points around the airfoil contour. The nondimensional wall distance ranged between  $30 \leq y^+ \leq 90$  for all 2D computations using scalable wall functions. The distance of the wall adjacent node was  $6.0E-04$  of the reference chord length off the wall; the following node was set at a distance of  $3.0E-04$  reference chord length from the first node followed by a grid expansion with factor 1.1. A variation in the normal grid spacing, i.e. wall adjacent node at  $3.0E-04$  reference chord length off the wall, altered results by less than 0.5% for both lift and drag coefficients. This shows that the scalable wall function approach gives consistent results. Furthermore, a grid convergence study has been performed, which is also illustrated in Fig. 6, showing differences in the lift coefficient between 1.5% and 3.5% and differences in the drag coefficient between 1.0% and 4.0% for the angles of attack considered. This serves as a good validation of the grid spacing of Fig. 5, as the local angle of attack does not exceed  $\alpha=20^\circ$  for the 3D calculations presented later in this work.

The average sectional Reynolds number of the NREL Phase VI Rotor is about  $Re=10^6$  over the entire power range. Experimental data is available from wind tunnels at Delft University of Technology (DUT) and Ohio State University (OSU), which are presented by Somers [20] and Reuss Ramsay et al. [21]. Experimental results for the lift and drag coefficients are shown in Figs. 7 and 8 along with PCS runs using  $k-\epsilon$  and  $k-\omega$  turbulence models as well as XFOIL by Drela [22]. It should be noted that clean experimental results are presented. The fully turbulent PCS runs are compared to clean experimental results in order to better ex-

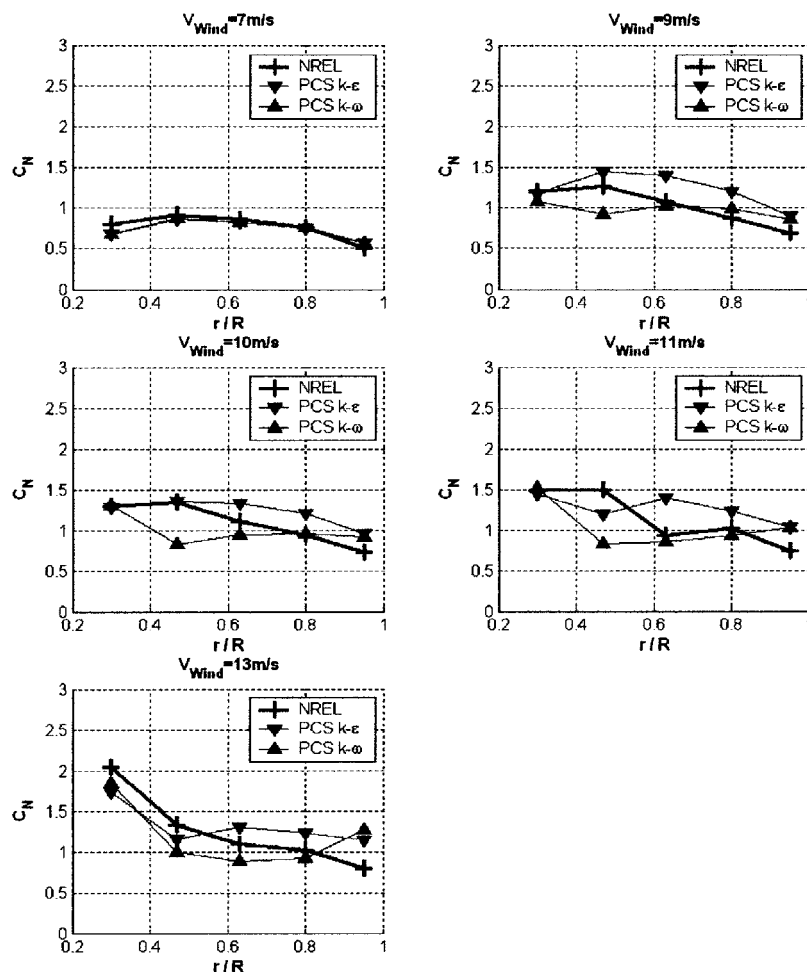


Fig. 14 Normal force coefficients (NREL phase VI, no yaw)

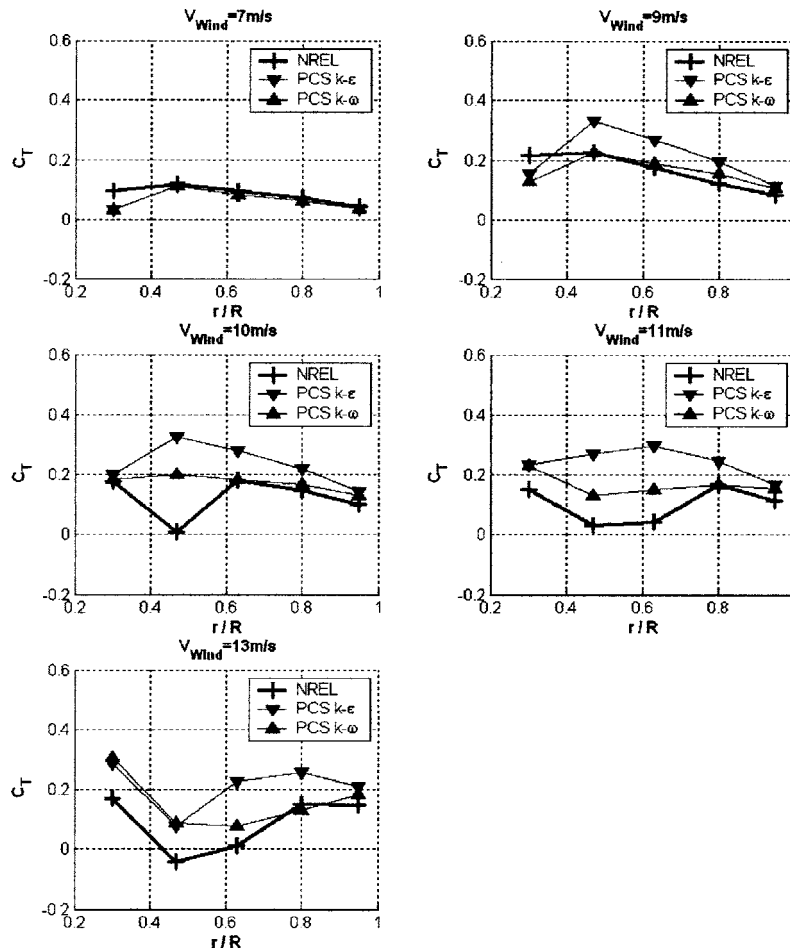


Fig. 15 Tangential force coefficients (NREL phase VI, no yaw)

plain the discrepancies that are found in 3D for the NREL Phase VI rotor. It can be seen in Fig. 7 that experimental data itself differs over the entire range of angles of attack, however, starts to deviate more significantly for  $\alpha > 18^\circ$ . Results obtained by XFOIL show best agreement with experimental data. As far as the PCS runs are concerned, the  $k-\omega$  model performs better than the  $k-\epsilon$  model. All codes agree well with experimental data of DUT for  $\alpha < 6^\circ$ , however, the PCS runs show larger drag coefficients in Fig. 8. This is in part attributed to the fully turbulent flow assumption of the PCS runs. On the other hand, experimental data [20,21] shows laminar flow over the forward half of the airfoil for  $\alpha < 5^\circ$ . The flow then undergoes “laminar” separation followed by a “turbulent” reattachment. Part of the discrepancy observed between experimental data and the PCS runs for separated flow and  $\alpha > 5^\circ$  can be attributed to delayed separation of turbulent boundary layers. XFOIL performs better because of its transition model; CFX V5.6 does not have a transition model. At  $\alpha = 9^\circ$ , experiments have shown that the laminar-turbulent transition point has moved forward and the airfoil experiences a small amount of turbulent trailing edge separation (5–10% of chord). As the angle of attack is further increased to  $\alpha = 15^\circ$ , the upper-surface transition point moves forward to the leading edge and the assumption of fully turbulent flow becomes more appropriate; the separated region moves forward to about the mid-chord. These observations coincide well with PCS  $k-\omega$  in Fig. 9, which shows contours of the  $U$  velocity component. Discrepancies between the  $k-\epsilon$  and  $k-\omega$  turbulence models are attributed to a different prediction of the onset of separation. This is also reflected by the lift coefficients in Fig. 7 and drag coefficients in Fig. 8. For the  $k-\omega$  turbulence

model, at angles of attack where flow separation occurs, the solution was converged up to a maximum residual of  $5 \times 10^{-4}$ .

**3D Calculations of the NREL Phase VI Rotor.** The PCS solver has been applied to the NREL Phase VI Rotor for wind speeds of  $V_{\text{Wind}} = 7, 9, 10, 11$ , and  $13$  m/s. Results obtained for the integrated rotor torque under no yaw conditions are shown in Fig. 10 along with results from a VLM model by Chattot [10,11]. It can be seen that PCS  $k-\omega$  runs show very good agreement with experiments, whereas VLM as well as PCS  $k-\epsilon$  runs overpredict rotor torque for wind speeds  $V_{\text{Wind}}$  above  $10$  m/s. The prediction of peak torque at  $V_{\text{Wind}} = 9$  m/s is difficult for all computational models. For the case of fully attached flow,  $V_{\text{Wind}} = 7$  m/s, all computational models agree very well with experimental data. This reveals three important facts:

1. A rigid wake in the VLM model is a good approximation in order to calculate induced velocities on the outer boundary of the Navier-Stokes zone.
2. The Coupling Methodology of combining a NS solver for the near-field with a VPM model for the far-field is validated.
3. Results are nearly identical for the  $k-\epsilon$  and  $k-\omega$  turbulence models for fully attached flow.

The authors have studied the influence of the number of vortex sheet revolutions in [23] and have found that convecting the vortex sheet for solely 1 to 2 revolutions into the wake alters the rotor torque prediction by 5%–10% compared to a very long wake with 20 revolutions plus the remainder terms. The authors want to emphasize once more that this is a main advantage of the PCS solver



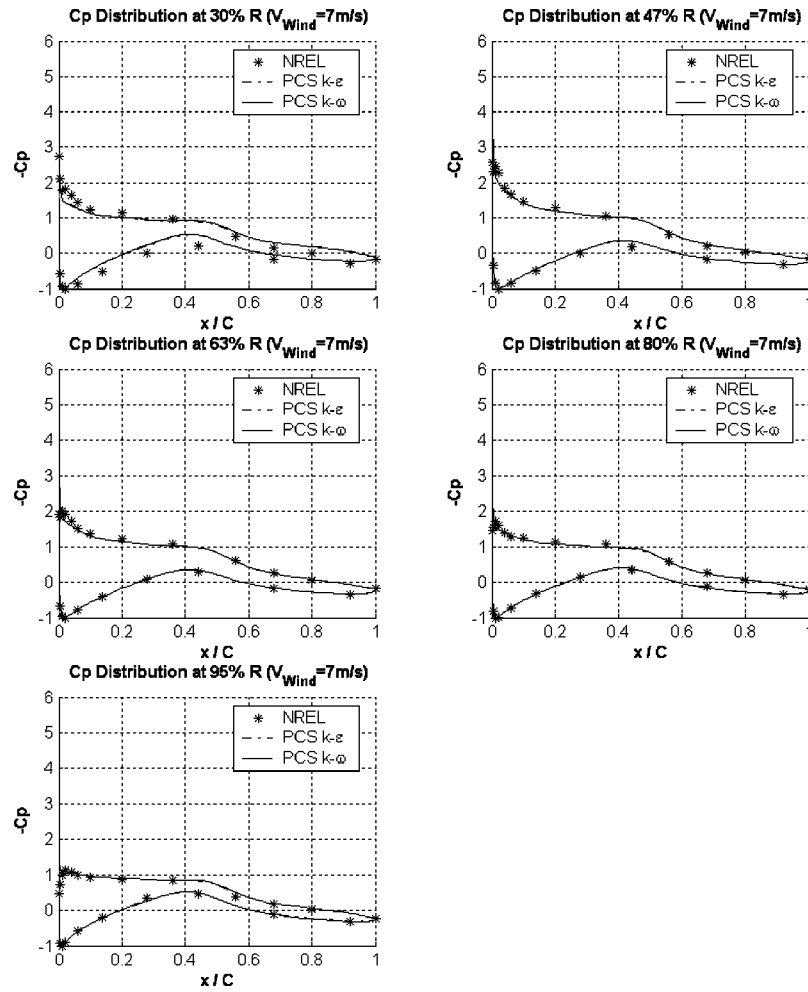


Fig. 16 Spanwise pressure coefficient ( $V_{\text{Wind}}=7$  m/s)

compared to a full-domain Navier-Stokes analysis that dissipates the vortex structure unphysically in the wake. Although full domain Navier-Stokes solutions in [3–5,8,9] give good results for fully attached flow under zero-yaw conditions, it is interesting to note that the number of vortex sheet revolutions does have influence on the flow solution. This will be investigated in future studies. Differences in rotor torque between the turbulence models in Fig. 10 for higher wind speeds can be related to some extent to differences in 2D behavior in Figs. 7 and 8 with respect to the onset of separation. This will be confirmed later by local pressure coefficients. Discrepancies in results for the VLM model for wind speeds  $V_{\text{Wind}} > 10$  m/s are attributed to 3D rotational separation phenomena along the blade, see Hallissy and Chattot [24]. The mesh alignment with the wake inside the Navier-Stokes zone plays a major role for the accuracy of the results. Figure 11 illustrates streamlines, which originate in front of the blade. The view is in direction of the trailing tip vortex. It can be seen though that the root vortex seems to trail downwards behind the blade. It becomes evident that for a good solution the grid inside the NS zone has to be capable of capturing the trailing vortices at root and tip. In order to accomplish this task, a rigid wake plane is created for each wind speed according to Eq. (4), upon which the C-type mesh around the blade is grown. This ensures to capture the vortex sheet in the best possible way with minimum grid size. Figure 12 shows an iso-vorticity surface around the rotor blade. It can be seen that trailing vorticity, i.e., the root vortex on the left and the tip vortex on the right as well as the vortex sheet, is well captured and preserved.

Local values for the nondimensional wall distance  $y^+$  are illustrated in Fig. 13 for  $V_{\text{Wind}}=7$  m/s and demonstrate the correctness of the near-wall grid.

Spanwise normal force coefficients are shown in Fig. 14 for wind speeds of  $V_{\text{Wind}}=7, 9, 10, 11$ , and 13 m/s. It can be seen that for  $V_{\text{Wind}}=7$  m/s the normal force coefficients of both turbulence models are nearly identical. However, the normal force coefficient at  $r/R=0.3$  is underpredicted. This is attributed to the fact that the root section is blunt, see Fig. 3(a), and the real pitch shaft section is not modeled at the present stage. For  $V_{\text{Wind}}=9$  m/s, separation occurs on the blade. Here, the  $k-\omega$  model is observed to predict better the normal force coefficients than the  $k-\epsilon$  model, however, with a distinct underprediction at  $r/R=0.47$ . For  $V_{\text{Wind}}=10$  and 11 m/s, differences between the turbulence models increase, the  $k-\omega$  model showing good agreement with NREL data at  $r/R=0.3, 0.63$ , and 0.8. Once more, the  $k-\omega$  model exhibits a large underprediction at  $r/R=0.47$ . For a wind speed of  $V_{\text{Wind}}=13$  m/s, results obtained by the  $k-\omega$  model follow well the trend of the experimental data except at the blade tip. It is interesting to note that both turbulence model agree well at the blade root  $r/R=0.3$  and at the blade tip  $r/R=0.95$  for all cases considered, but exhibit large discrepancies at the intermediate stations  $r/R=0.47, 0.63$  and 0.8 for  $V_{\text{Wind}} > 7$  m/s where the flow is partially separated and stalled. This reveals the effect of the turbulence model on results, see also Benjanirat et al. [7]. Moreover, the overprediction at the blade tip increases with wind speed. Although the



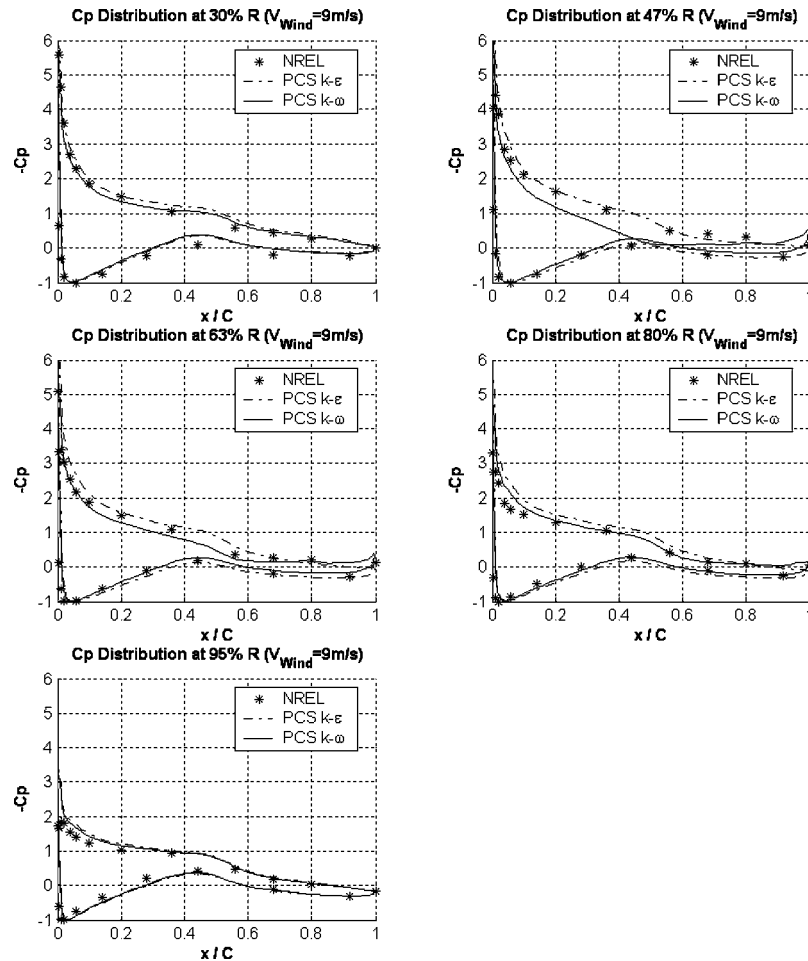


Fig. 17 Spanwise pressure coefficient ( $V_{\text{Wind}}=9$  m/s)

$k-\omega$  model predicts the rotor torque very well in Fig. 10, the  $r/R=0.47$  station is poorly predicted in Fig. 14. This reveals once more that the underlying flow physics is very complex.

As far as spanwise tangential force coefficients are concerned, they are shown in Fig. 15. It can be seen that for wind speeds of  $V_{\text{Wind}}=7$  and 9 m/s PCS  $k-\omega$  results follow very well the trend of the experimental data, whereas PCS  $k-\epsilon$  results show a more significant overprediction for  $V_{\text{Wind}}=9$  m/s. Again, the  $r/R=0.3$  station is underpredicted, which is attributed to the blunt tip shape at the root section. This will be revealed later by local pressure coefficients. A different behavior is observed for wind speeds of  $V_{\text{Wind}}=10, 11$  and 13 m/s. Here, PCS results show larger discrepancies compared with experimental data. It seems that at inboard stations with flow separation, the PCS runs overpredict tangential blade loads to a larger extent than where the flow is fully attached. Once more the  $k-\omega$  model gives better results than the  $k-\epsilon$  model. The sectional pressure coefficients in Figs. 16–18 explain the discrepancies observed. For the case of fully attached flow,  $V_{\text{Wind}}=7$  m/s in Fig. 16, sectional pressure coefficients agree very well with experimental data except at the blade root at  $r/R=0.3$ . Here, the effect of the blunt tip shape in Fig. 3(a) can be directly seen in the pressure coefficients. Figure 17 illustrates sectional pressure coefficients for a wind speed of  $V_{\text{Wind}}=9$  m/s. At  $r/R=0.47, 0.63, 0.8$  and approximately 70% local chord, the NREL data shows boundary layer separation with regard to a discrimination criterion defined by Schreck and Robinson in [25,26]. Both turbulence models show reasonable agreement with the NREL data except for the  $k-\omega$  model at  $r/R=0.47$  exhibiting a larger separated flow region. Schreck and Robinson [25,26] differentiate be-

tween two flow field topologies for separated flow of the NREL Phase VI Rotor, boundary layer separation and shear layer impingement. They revealed that boundary layer separation is followed by shear layer impingement at higher wind speeds. Figure 18 illustrates shear layer impingement for the NREL data at  $r/R=0.30$  and 0.47 at a wind speed of  $V_{\text{Wind}}=10$  m/s. It can be seen though that the PCS runs fail to predict the local pressure coefficient at these radial stations, in particular at  $r/R=0.47$ . This is also reflected in the tangential force coefficients in Fig. 15. The reason for the discrepancies is due to the fact that shear layer impingement is related to laminar flow separation near the leading edge, which cannot be predicted with the fully turbulent flow assumption in the PCS runs. On the other hand, the PCS runs show once more reasonable agreement with NREL data at  $r/R=0.63, 0.8$ , and 0.95. It can be observed though in Fig. 18 that the PCS  $k-\omega$  results exhibit some convergence problems at the trailing edge. This has been already observed for the 2D S809 results and is attributed to the fact that a steady-state solution is sought, while the flow field might be essentially unsteady.

The difference in rotor torque in Fig. 10 between the  $k-\epsilon$  and  $k-\omega$  turbulence model is due to the difference in blade loads and pressure coefficient for  $0.47 < r/R < 0.95$ . This difference is related to the prediction of the onset of separation, which has been observed earlier for 2D calculations in Figs. 7 and 8. It reveals once more that the turbulence model becomes very important for the accurate prediction of rotor torque at higher wind speeds. The authors want to emphasize that although the  $k-\omega$  turbulence model

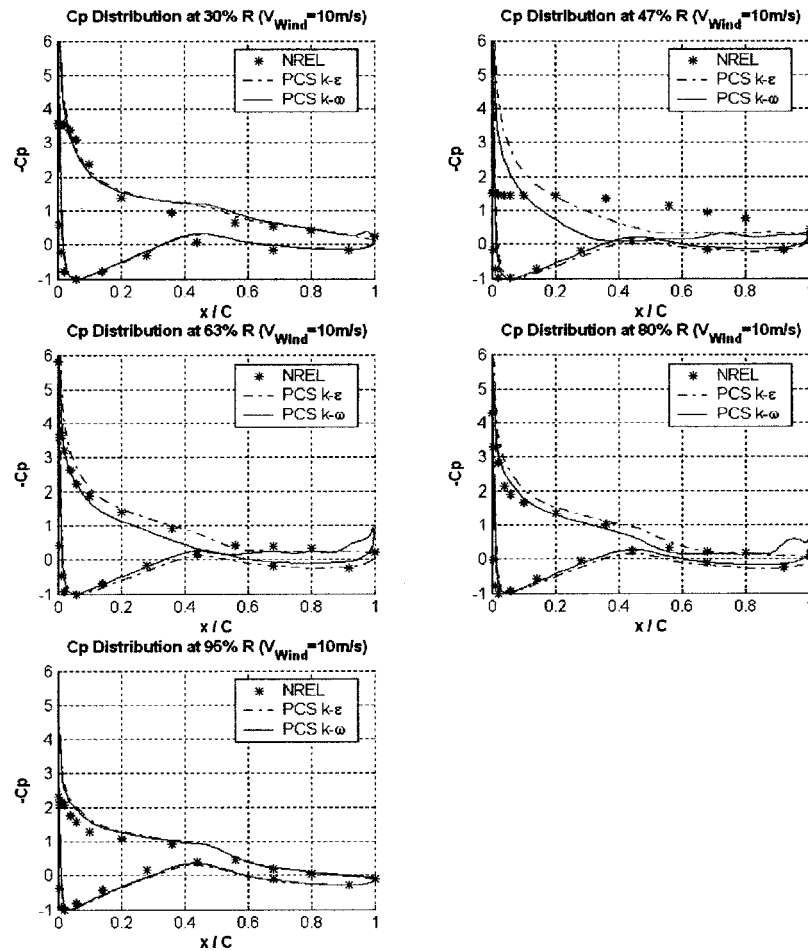


Fig. 18 Spanwise pressure coefficient ( $V_{\text{Wind}}=10$  m/s)

predicts rotor torque in Fig. 10 quite well, it can be seen in Figs. 17 and 18 that local pressure coefficients differ substantially from NREL data at certain radial stations.

**3D Vortex Tube at Peak-Power.** In 2000, Schreck et al. [27] analyzed experimental data of the NREL Phase IV Rotor in order to gain a deeper understanding of wind turbine blade aerodynamics in yawed flow under high load conditions. The main focus of their work was to portray the physics of 3D, unsteady, vortical flows that lead to normal force amplification and delayed stall. Measured surface pressure histories were used to characterize such dynamic stall vortices. They found that a dynamic stall vortex generates a region of low pressure on the lifting surface, and thus results in a lift amplification exceeding that of 2D experimental data. At the same time, Sorensen [28] observed this complex flow structure in a full domain NS analysis of the NREL Phase VI Rotor at higher wind speeds and visualized it by means of iso-vorticity surfaces behind the rotor. In 2002, Johansen et al. [29] documented an unstable inboard vortex for the parked NREL Phase VI Rotor using Detached-Eddy Simulation (DES). Recently, Tangler et al. [30] sought a deeper insight into the flow physics occurring at peak-power of the NREL Phase VI Rotor under steady and zero-yaw conditions. They used NREL's Lifting Surface Prescribed Wake Code (LSWT) and adjusted 2D polar data  $C_l$  and  $C_d$  in order to match results obtained with measured normal force coefficient  $C_N$  and tangential force coefficient  $C_T$  at five radial stations. This enabled them to also predict the blade's angle of attack distribution. Furthermore, Tangler et al. [30] observed a rapid drag increase at  $r/R=0.47$  just after peak-power and associated this with the bursting of a standing spanwise vortex

from the lifting surface.

The coupling methodology of the PCS solver in Fig. 2 directly relates gradients in the spanwise distribution of circulation  $\Gamma_j$  to trailing vorticity  $\delta\Gamma_j$ , which is convected downstream of the blade without numerical dissipation. Large values of  $\delta\Gamma_j$  are associated with concentrated vorticity. Figure 19 illustrates the spanwise dis-

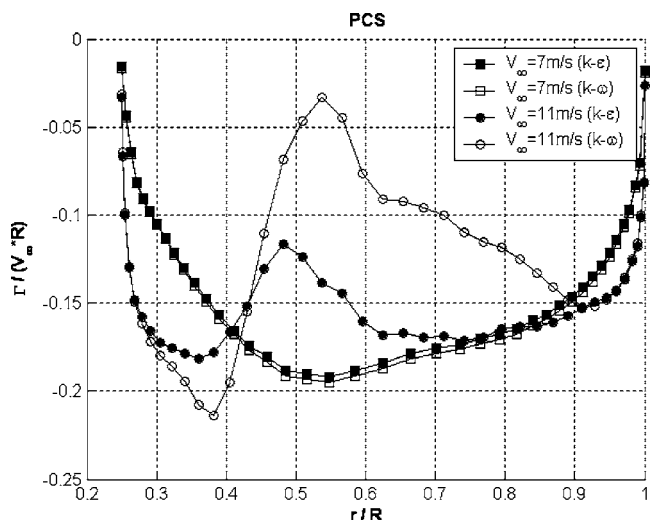


Fig. 19 Spanwise circulation distribution

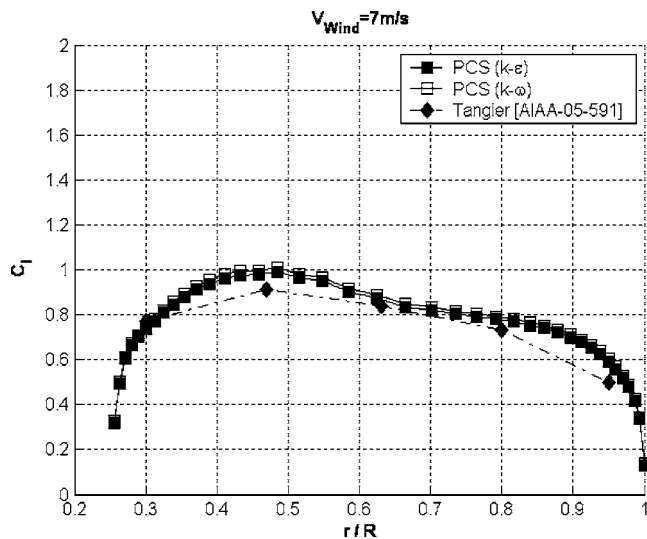


Fig. 20 Spanwise lift coefficient ( $V_{\text{Wind}}=7$  m/s)

tribution of circulation  $\Gamma_j$  for PCS runs at  $V_{\text{Wind}}=7$  and 11 m/s. Good agreement is found between the two turbulence models for fully attached flow at  $V_{\text{Wind}}=7$  m/s. At the higher wind speed of  $V_{\text{Wind}}=11$  m/s, large discrepancies are apparent between the two turbulence models, which are also reflected in the normal and tangential force coefficients in Figs. 14 and 15 and are attributed to different prediction of the onset of separation. This has been discussed earlier for 2D results in Figs. 7 and 8. Figure 19 reveals the presence of concentrated trailing vorticity on the blade. It can be seen that this trailing vorticity is counter-rotating to the root vortex. The authors prefer to term this phenomenon as a vortex “tube” rather than a vortex, as the spanwise extent is larger than that of the root and tip vortices, see Fig. 19. It seems that the vortex tube extends from  $r/R \approx 0.38$  to  $r/R \approx 0.52$ . Rosenhead [31] describes such 3D flow topographies as spiral separation, which can even occur in ordinary flow over swept-back wings. A free shear or vortex layer due to spiral separation shows a highly three-dimensional flow pattern. Rosenhead [31] concludes that the shear or vortex layer can be regarded as a vortex sheet in its effects on the surrounding main stream. This is exactly how the coupling methodology in Fig. 2 treats trailing vorticity. As far as the local lift coefficients  $C_l$  are concerned, they are shown in Figs. 20 and 21 for the PCS runs and Tangler et al. [30]. The  $C_l$  values for the PCS results were obtained using the Kutta-Joukowski lift theorem as  $C_l(j) = -2\Gamma_j / (U_\infty(j) \cdot c(j))$ , where  $c(j)$  is the local chord length and  $U_\infty(j)$  is the local free stream speed obtained from the ambient pressure  $p_\infty$  and the local stagnation pressure  $p_{\text{stag}}(j)$  using the incompressible Bernoulli equation. It should be mentioned that this is not an exact statement for viscous flow, however it is a good approximation along the stagnation streamline. Figure 20 shows very good agreement between PCS results and those of Tangler et al. [30] at  $V_{\text{Wind}}=7$  m/s. It has to be kept in mind though that results presented in [30] do not strictly account for local 3D boundary layer effects, as the LSWT code is based on strip theory. Moreover, results are matched at only five radial stations where experimental data is available. This gives some uncertainty in the results presented in [30]. Two-dimensional wind tunnel test data in [20,21] and Fig. 7 showed a maximum lift coefficient of  $C_{l,\text{max}} \approx 1.1$  for the S809 airfoil. Figure 21 clearly illustrates lift coefficients beyond the 2D  $C_{l,\text{max}}$  at  $V_{\text{Wind}}=11$  m/s. A comparison with Tangler et al. [30] is difficult. It seems though that the spanwise vortex tube is located further inboard for the PCS runs. Moreover, the tip region shows fairly large values for the lift coefficient in the PCS runs compared to data presented in [30]. Figure 22 visualizes the spanwise vortex

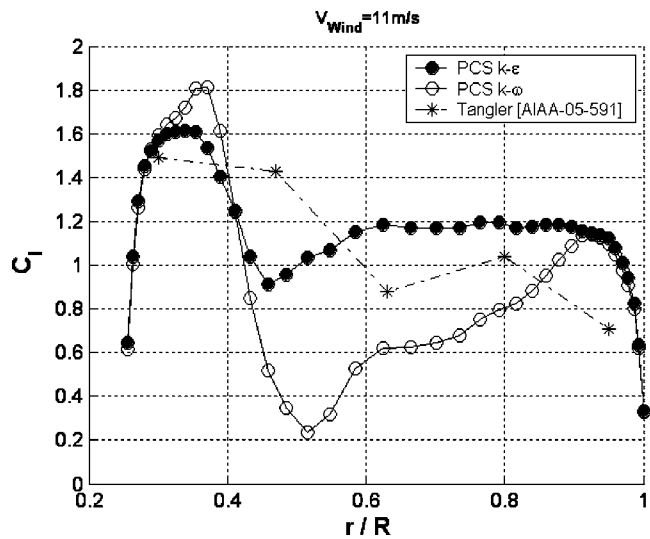


Fig. 21 Spanwise lift coefficient ( $V_{\text{Wind}}=11$  m/s)

tube at a wind speed of  $V_{\text{Wind}}=11$  m/s. The view is looking down on the upper or lifting surface of the blade with the blade root on the left and the blade tip on the right. Root and tip vortices are seen as confined vortical structures, whereas the spanwise vortex tube is more diffused and part of the inboard vortex sheet.

## Summary and Conclusions

A Navier-Stokes solver, CFX V5.6, has been successfully coupled with an in-house developed Vortex Panel Method and parallelized on a cluster of 4 processors. The main objective of the coupling methodology is to better represent the trailing vortex wake behind wind turbines, thus reducing artificial dissipation, which is inevitable when using Navier-Stokes solvers. The coupled solver combines the strengths of two methods, namely resolving 3D flow features in the immediate vicinity of the blade by a Navier-Stokes solver and accounting for the trailing vortex wake by using a vortex method, which is dissipation free.

The Parallelized Coupled Solver (PCS) has been applied to the NREL Phase VI Rotor configuration at various wind speeds,  $V_{\text{Wind}}=7,9,10,11$ , and 13 m/s, with and without flow separation under steady and no-yaw conditions. Runs took approximately 4 h of wall-clock time on a cluster of four processors. The relatively small size of the NS zone around the rotor blade makes this method computationally much more efficient than a full-domain Navier-Stokes analysis, e.g., [3–5,8,9].

Some further characteristics of the Parallelized Coupled Solver can be summarized as:

1. A “rigid” wake is responsible for a robust solver.



Fig. 22 Isosurface of vorticity ( $V_{\text{Wind}}=11$  m/s)

- The modeling of the entire vortex sheet enables the solver to convect inboard trailing vorticity, such as a vortex tube, into the wake.
- The capture of the vortex sheet inside the Navier-Stokes zone is improved by aligning the Navier-Stokes grid with the rigid wake.

Two turbulence models were compared in the analysis, the  $k-\varepsilon$  and  $k-\omega$  two-equation models. The  $k-\omega$  model showed good agreement with experimental data obtained in the NASA Ames Wind Tunnel for the rotor torque, however some discrepancies in spanwise normal and tangential force coefficients were observed and discussed in detail. The  $k-\varepsilon$  model showed good agreement for fully attached flow and overpredicted rotor torque for partially separated flow. Differences between the turbulence models were attributed to the prediction of the onset of separation, which was supported by 2D S809 airfoil analysis. All runs assumed fully turbulent flow, as the version of the Navier-Stokes solver, CFX 5.6, did not provide a transition model. However, the NREL experiments showed transitional flow and its influence on local pressure distributions and power predictions.

The PCS runs give promising results considering the computational savings. Furthermore, the solver discloses a complex spanwise vortex tube through the coupling methodology. Nevertheless, the solver exhibited some limits with respect to steady and fully turbulent flow assumptions. The performance prediction of stall-controlled wind turbines still faces many challenges today. The coupling methodology presented in this work demonstrated its potential in disclosing complex flow phenomena currently not well understood.

## Nomenclature

$a, b, c$	= Geometric influence coefficients, $m^{-1}$
$adv$	= Advance Ratio, $V/(\Omega R)$
$c$	= Local blade chord, m
$C_L$	= Lift coefficient
$C_N$	= Normal force coefficient
$C_p$	= Pressure coefficient
$C_T$	= Tangential Force coefficient
$d$	= Differential operator
$ix$	= Number of segments of each helicoidal vortex filament
$jx$	= Number of vortex filaments along blade
$kx$	= Number of segments of each bound vortex filament
$L$	= Contour line, m
$\mathbf{l}$	= Length of vortex filament segment, Vector
$Q$	= Stagnation point dynamic pressure, Pa
$R$	= Rotor Radius, m
$r$	= Local Radius, m
$\mathbf{r}$	= Position Vector
$S$	= Total Arc Length of Profile Contour
$u, v, w$	= Cartesian velocity components, $m\ s^{-1}$
$U_\infty$	= Local free stream speed, $m\ s^{-1}$
$V_{Wind}$	= Wind Speed, $m\ s^{-1}$
$\mathbf{v}_c$	= Induced velocity vector at arbitrary point C
$x, y, z$	= Cartesian coordinates, m, m, m
$y^+$	= Nondimensional wall distance
$\alpha$	= Angle of attack, rad
$\Gamma_j$	= Spanwise Circulation, $m^2\ s^{-1}$
$\Delta$	= Incremental quantity
$\Delta s/S$	= Grid Spacing along profile contour
$\delta\Gamma_j$	= Local vortex strength, $m^2\ s^{-1}$
$\varphi$	= Phase angle of trailing edge, rad
$\Theta$	= Vortex segmentation angle, rad
$\rho$	= flow density, $kg\ m^{-3}$
$\Omega$	= Angular rotor speed, $rad\ s^{-1}$
$\omega$	= Vorticity, $s^{-1}$

## Indices

$B$	= Blade
bound	= Bound Vortex
$C$	= Arbitrary Point C
helix	= Helicoidal Vortex Sheet
$i$	= Location on Helicoidal Vortex Filament
$j$	= Spanwise Location on Blade
$k$	= Location on Bound Vortex Filament
rem	= Remainder Term
$T$	= Trefftz Plane
$TE$	= Trailing Edge

## Abbreviations

AM	= Aeroelastic Model
BEM	= Blade Element Method
DES	= Detached-Eddy Simulation
DUT	= Delft University of Technology
LSWT	= NREL's Lifting Surface Prescribed Wake Code
NREL	= National Renewable Energy Laboratory
NS	= Navier-Stokes
OSU	= Ohio State University
PCS	= Parallelized Coupled Solver
UAE	= Unsteady Aerodynamic Experiment
VLM	= Vortex Line Method
VPM	= Vortex Panel Method
WM	= Wake Model

## References

- [1] Fingersh, L. J., Simms, D., Hand, M., Jager, D., Cotrell, J., Robinson, M., Schreck, S., Larwood, S., 2001, "Wind Tunnel Testing of NREL's Unsteady Aerodynamics Experiment," AIAA-2001-0035, pp. 194–200.
- [2] Simms, D., Schreck, S., Hand, M., Fingersh, L. J., 2001, "NREL Unsteady Aerodynamics Experiment in the NASA-Ames Wind Tunnel: A Comparison of Predictions to Measurements," NREL/TP-500-29494.
- [3] Sorensen, N. N., 2000, "Evaluation of 3D effects from 3D CFD computations," IEA Joint Action, *Aerodynamics of Wind Turbines, 14<sup>th</sup> Symposium*, Boulder CO.
- [4] Sorensen, N. N., Michelsen, J. A., Schreck, S., 2002, "Navier-Stokes Predictions of the NREL Phase VI Rotor in the NASA Ames 80 ft  $\times$  120 ft Wind Tunnel," *Wind Energy*, **5**, pp. 151–169.
- [5] Sorensen, N. N., Michelsen, J. A., Schreck, S., 2002, "Application of CFD to Wind Turbine Aerodynamics," GRACM 2002, Patra.
- [6] Xu, G., Sankar, L., 2002, "Application of a Viscous Flow Methodology to the NREL Phase VI Rotor," AIAA-2002-0030, 40<sup>th</sup> AIAA Aerospace Sciences Meeting and Exhibit, Reno NV.
- [7] Benjanirat, S., Sankar, L., Xu, G., "Evaluation of Turbulence Models for the Prediction of Wind Turbine Aerodynamics," AIAA-2003-0517, 41<sup>st</sup> AIAA Aerospace Sciences Meeting and Exhibit, Reno NV, 2003.
- [8] Le Pape, A., Lecanu, J., 2004, "3D Navier-Stokes Computations of a Stall-regulated Wind Turbine," *Wind Energy*, **7**, pp. 309–324.
- [9] Duque, E. P. N., Burklund, M. D., Johnson, W., 2003, "Navier-Stokes and Comprehensive Analysis Performance Predictions of the NREL Phase VI Experiment," *J. Sol. Energy Eng.*, **125**, pp. 457–467.
- [10] Chattot, J. J., 2002, "Design and Analysis of Wind Turbines Using Helicoidal Vortex Model," *Comput. Fluid Dyn. J.*, **11**, pp. 50–54.
- [11] Chattot, J. J., 2004, "Helicoidal Vortex Model for Steady and Unsteady Flows," AIAA 2004-0829, 23<sup>rd</sup> ASME Wind Energy Symposium, Reno NV.
- [12] Tangler, J. L., 2002, "The Nebulous Art of Using Wind-Tunnel Airfoil Data for Predicting Rotor Performance," NREL/CP-500-31243.
- [13] Steinhoff, J., Underhill, D., 1994, "Modification of the Euler Equations for "Vorticity Confinement": Application to the computation of interacting vortex rings," *Phys. Fluids*, **6**, pp. 2738–2744.
- [14] Schmitz, S., Chattot, J. J., "A Coupled Navier-Stokes/Vortex-Panel Solver for the Numerical Analysis of Wind Turbines," *Proceedings of the International Conference on CFD 3, Toronto*, Springer-Verlag (to be published).
- [15] Benjanirat, S., Sankar, L. N., 2004, "Recent Improvements to a Combined Navier-Stokes Full Potential Methodology for Modeling Horizontal Axis Wind Turbines," AIAA-2004-0830, 23<sup>rd</sup> ASME Wind Energy Symposium, Reno NV.
- [16] Grotjans, H., Menter, F. R., 1998, "Wall Functions for General Application CFD Codes," *ECCOMAS 98 Proceedings of the Fourth European Computational Fluid Dynamics Conference*, John Wiley and Sons, pp. 1112–1117.
- [17] Karypis, G., Kumar, V., 1996, "Parallel Multilevel k-way Partitioning Scheme for Irregular Graphs," University of Minnesota, Department of Computer Science, Technical Report 96-036.
- [18] Gupta, S., Leishman, J. G., 2004, "Accuracy of the Induced Velocity of Wind Turbine Wakes Using Vortex Segmentation," AIAA-2004-0828, 23<sup>rd</sup> ASME Wind Energy Symposium, Reno NV.
- [19] Wolfe, W. P., Ochs, S. S., 1997, "CFD Calculations of S809 Aerodynamic



- Characteristics," AIAA-97-0973, *35<sup>th</sup> Aerospace Sciences Meeting and Exhibit*, Reno NV.
- [20] Somers, D. M., 1997, "Design and Experimental Results for the S809 Airfoil," NREL/SR-440-6918.
- [21] Reuss Ramsay, R., Hoffmann, M. J., Gregorek, G. M., 1995, "Effects of Grit Roughness and Pitch Oscillations on the S809 Airfoil," NREL/TP-442-7817.
- [22] Drela, M., "XFOIL: An Analysis and Design System for Low Reynolds Number Airfoils," *Conference on Low Reynolds Number Aerodynamics*, in "Low Reynolds Number Aerodynamics," T. J. Mueller (editor), Lecture Notes in Engineering No. 54, Springer Verlag.
- [23] Schmitz, S., Chattot, J. J., "Influence of the Vortical Wake behind Wind Turbines Using a Coupled Navier-Stokes/Vortex-Panel Methodology," *Proceedings of the Third M. I. T. Conference on Computational Fluid and Solid Mechanics*, Boston, Elsevier (to be published).
- [24] Hallissy, J. M., Chattot, J. J., 2005, "Validation of a Helicoidal Vortex Model with the NREL Unsteady Aerodynamic Experiment," AIAA-2005-1454, *24<sup>th</sup> ASME Wind Energy Symposium*, Reno NV.
- [25] Schreck, S., Robinson, M., 2003, "Boundary Layer State and Flow Field Structure Underlying Rotational Augmentation of Blade Aerodynamic Response," J. Sol. Energy Eng., **125**, pp. 448–456.
- [26] Schreck, S., Robinson, M., 2005, "Unsteadiness in HAWT Blade Aerodynamic Forces and Flow Field Structures During Rotational Augmentation," AIAA-2005-0776, *24<sup>th</sup> ASME Wind Energy Symposium*, Reno NV, 2005.
- [27] Schreck, S., Robinson, M., Hand, M., Simms, D., 2000, "HAWT Dynamic Stall Response Asymmetries Under Yawed Flow Conditions," NREL/CP-500-27898.
- [28] Sorensen, N. N., "Evaluation of 3D effects from 3D CFD computations," IEA Joint Action, *Aerodynamics of Wind Turbines, 14<sup>th</sup> Symposium*, Boulder CO, 2000.
- [29] Johansen, J., Sorensen, N. N., Michelsen, J. A., Schreck, S., "Detached-Eddy Simulation of Flow around the NREL Phase-VI Blade," AIAA-2002-0032, *40<sup>th</sup> AIAA Aerospace Sciences Meeting and Exhibit*, Reno NV, 2002.
- [30] Tangler, J., Kocurek, J. D., "Wind Turbine Post-Stall Airfoil Performance Characteristics Guidelines for Blade-Element Momentum Methods," AIAA-2005-0591, *24<sup>th</sup> ASME Wind Energy Symposium*, Reno NV, 2005.
- [31] Rosenhead, L., 1963, *Laminar Boundary Layers*, Oxford University Press, pp. 75–77, 488–491.